In situ neutron diffraction in quantifying deformation behaviors of nano-sized carbide strengthened UFG ferritic steel

J.W. Liang[1], Y.F. Shen[*, 1], C.S. Zhang[2], X. W. Feng[3], H.B. Wang[3], X. Sun[*, 4]

1. School of Materials Science and Engineering, Northeastern University, Shenyang, 110819, China
2. Key Lab for Neutron Physics of the Chinese Academy of Engineering Physics, Institute of Nuclear Physics and Chemistry, Mianyang, 621999, China
3.General Engineering Research Institute of the Chinese Academy of Engineering Physics, Mianyang, 621999, China
4. Oak Ridge National Laboratory, Oak Ridge, TN 37930, U.S.A.

Abstract

The microstructures and mechanical properties of a low-alloy medium-carbon steel with a duplex microstructure composed of nanoscale spheroidized carbides in ultrafine-grained (UFG) ferritic steel are examined. The average grain size of the studied steel is ~ 430 nm, and these grains coexist with numerous carbides. Neutron diffraction reveals that the intensity of (011) and (022) peaks for the UFG sample is significantly enhanced, suggesting that the (011)//RD texture is a result of the warm rolling process. The lattice parameter of UFG steel is smaller than that of a martensitic steel (M steel) counterpart, indicating a lower carbon concentration in the lattice. The estimated dislocation densities for M steel and UFG steel are 2.59×10^{14} cm^{-2} and 1.76×10^{12} cm^{-2}, respectively. The UFG steel reveals a nearly isotropic lattice strain response under initial tension from 0 to 450 MPa, where the lattice strains of the (110), (002), and (112) planes are identical. The increase of lattice strain of the (110) plane becomes smaller than that of the (002) and (112) planes as the stress exceeds 450 MPa, suggesting that the nanosized carbides contribute to the hardening ability by promoting the accumulation of geometrically necessary dislocations around the particles, and the (110) lattice becomes harder compared to the other two planes.

Keywords： ultrafine-grained ferritic steel; nanosized carbides; strength; neutron diffraction

* Corresponding authors: yfshen@neu.edu, sunx1@ornl.gov

1. Introduction

Metals can be strengthened through the controlled creations of internal defects and boundaries that obstruct dislocation motion, thereby enhancing their strength, ductility, and toughness [1, 2]. Grain refinement has been demonstrated as an effective method for strengthening metals, in the meantime, it can also result in a decrease in ductile-to-brittle transition temperature [3, 4]. Improvements in strength and toughness have been achieved in a low-alloy steel containing ultrafine, elongated ferrite grains strengthened with nanosized carbides [2]. In another example, ultrafine-grained (UFG) 0.2% C–Mn steel consisting of spheroidized cementite particles in an ultrafine ferrite matrix (~1.3 μm) showed an improved combination of strength and toughness compared with a corresponding coarse-grained (CG) counterpart [5]. The cementite is hard and brittle, and the spheroidized microstructure, which consists of a plate-type lamellar cementite and ferrite matrix, offers high ductility due to the soft ferrite matrix [6]. Among various microstructures of steels, those with spheroidized carbide particles embedded in a ferrite matrix show high ductility [7, 8], and the superior ductility of these steel plays an important role in the cold rolling and cold forming of low and medium carbon steels and in the machinability of high-carbon steels before the final hardening processes [5].

D6AC steel is a medium low-alloy carbon steel featuring a carbon content of 0.42–0.48 wt. % with several other elements within the ranges specified by Aerospace Material Specification (AMS) 6431 standard, i.e., 0.9–1.2 Cr, 0.9–1.1 Mo, 0.4–0.7 Ni, 0.08–0.15 V, 0.6–0.9 Mn, and 0.15–0.3 Si, in wt. %. The chemical composition of

D6AC steel is similar to that of AISI4340 and AISI 4140, but it also contains additional V and Cu, which are a strong carbide-forming element and a solid solution strengthening element, respectively. D6AC has high strength and a high yield-to-tensile strength ratio and is widely used in pressure vessels and aerospace and defense components [9–11]. However, wider utilization of this steel is limited by its poor ductility at high strength levels [12, 13]. Several studies on the fracture of D6AC steel have been reported [14, 15], and the mechanical properties of D6AC may vary considerably depending on its subsequent annealing treatment [16–18]. The key challenge is that its increased brittleness upon prior cold working dramatically decreases the steel's toughness as well as formability [19]. The typical heat treatment of D6AC steel typically involves direct quenching from a high austenitic temperature to room temperature, followed by conventional tempering [6]. This process is typically referred to as spheroidization treatment in steels in order to obtain uniformly distributed spheroidized carbide particles, i.e., cementite (Fe_3C), in a ferrite matrix, with the intention to improve the toughness and ductility of this type of steels.

The spheroidized microstructure is formed at a certain temperature for a sufficiently long holding time for the desired level of carbon diffusion reaction to take place. It has been reported that the spheroidization of the cementite can improve mechanical properties, including hardness [5, 20] and toughness. The improved toughness of the spheroidized microstructure may be attributed to the presence of finely dispersed cementite particles, which increase the work hardening rate by promoting the accumulation of geometrically necessary dislocations around the particles [5, 21]. In a

previous study, ultrafine-grained, low-alloy, medium-carbon steel was successfully prepared and revealed an ultrahigh tensile strength of 1260 MPa and a good ductility of 15% [22]. The ultrahigh strength–ductility combination was mostly attributed to the nanoscale spheroidized cementite that resulted from innovative processing [22], but the detailed deformation mechanisms and the extent the cementite's contribution to this strength have not been quantified.

Neutron diffraction has been used extensively to study the mechanical behaviors of structural materials because of its nondestructive approach to quantitatively determining elastic lattice strains. For example, in situ neutron diffraction experiments performed during tensile tests have revealed different work hardening behaviors in the ferrite-cementite steels [23]. In situ tensile deformation of a 1% CrMoV bainitic steel using synchrotron and neutron diffraction has demonstrated the evolution of internal micro-stresses and the load-sharing mechanisms among the ferrite matrix and the various carbides [24]. Cementite shows elastic anisotropic behavior and starts to share load from the ferrite matrix at the onset of macroscopic plastic deformation. By using in situ neutron diffraction, stress–strain relationships have been quantified for ferrite and martensite [25] in a dual-phase steel and for ferrite and austenite [26] in a duplex stainless steel, revealing that the crystallographic orientation of the ferrite phase significantly affects shear strain localization and void initiation in the ferrite regions adjacent to the hard phases during uniaxial tension [25].

This study mainly focused on characterizing the microstructures and understanding the deformation mechanisms of the UFG D6AC steel with in situ

neutron diffraction during uniaxial tensile deformation. The effect of UFG and nanoscale particles on the strength and ductility of the low-alloyed steel was quantitatively explored using in situ neutron diffraction. For reference, the as-prepared CG steel was annealed and quenched to obtain a fully martensitic microstructure, referred here within as M steel. The M-steel has low ductility and exhibits catastrophic fracture in tensile test due to its fully martensitic microstructure.

Postmortem transmission electron microscopy (TEM) was also used to characterize the relationship between mechanical properties and microstructures, in an attempt to discern the relationship between stress/strain and microstructures during the deformation process of the investigated steel. This study aims to provide quantitative insights into the deformation mechanisms of the UFG steels strengthened with nanoscale precipitates. Coupled with future reaction diffusion studies, these results may provide new insights in the design and development of new processing routes for improved properties of this class of steels.

2. Experimental procedures

2.1. Specimen preparation

The alloy was melted in a vacuum induction furnace, and an ingot was casted ($300 \times 200 \times 20$ mm^3). The chemical composition, measured by inductively coupled plasma mass spectroscopy, is listed as follows: 1.05Cr, 1.01Mo, 0.73Mn, 0.61Ni, 0.17Si, 0.09V, 0.43C (in wt.%), and balanced with Fe. A plate was cut from the ingot, homogenized in an air furnace at 1200°C for 2 hrs to remove the inhomogeneous microstructures evolved during solidification, hot rolled at 950°C in nine passes to a

thickness of 6.5 mm (ε = 85%), and then annealed at 800°C for 2 hrs and subsequently cooled to room temperature in air. The resulting steel was designated as CG-steel. Subsequently, the plate was annealed at 750°C for 300s, followed by warm rolling at 750°C for six passes plus annealing at 550°C for 300s after each pass to achieve to a final thickness of 2 mm. The resulting specimen was designated as UFG steel. To quantify the strengthening effects of grain refinement and nanosized precipitates, a fully martensitic microstructure (designed as M steel) was obtained by annealing the CG steel at 850°C for 1 hr and then quenching it to room temperature with water.

2.2. Microstructure characterization

To determine the volume fraction of carbides, X-ray diffraction (XRD) analysis was performed using an X'Pert PRO diffractometer (PW3040/60, Panalytical B.V., Netherlands) with monochromated CuKα (wavelength λ=0.1542nm) and an X-ray detector, operating at 40 kV and 40 mA. The XRD data were collected over a 2θ range from 10° to 120° at a scanning speed of 0.02 °/s. X-ray profile refinements were used to determine the volume fraction of carbides using the integrated intensities of carbide peaks and (200), (211), and (220) peaks of ferrite with the following equation [27]:

$$V_c = 1.4I_c / (I_\alpha + 1.4I_c) , \quad (1)$$

where V_c is the volume fraction of carbides, and I_c and I_α are the average integrated intensity of the carbide peaks and average integrated intensities of the ferrite peaks, respectively.

Using scanning electron microscopy (SEM) in conjunction with electron backscatter diffraction (EBSD), the grain morphology of the as-prepared steel was characterized prior to straining. The specimens were mechanically polished and finally electropolished at 20V for 15s to remove the surface damage from grinding and mechanical polishing. The electrolyte consisted of 10 vol. % perchloric acid and 90 vol. % ethanol. The EBSD data were collected using a SU-70 Hitachi field-emission scanning electron microscope with an acceleration voltage of 20 kV and a sample tilt angle of 70^{o}. The selected scanning step was 0.1 μm and an analyzed area of 1.5 × 1.0 mm^2 were used to ensure statistical representativeness. The acquired data were analyzed using OIM software.

Specimens for TEM analysis were cut from the homogeneously deformed regions close to the failure surface (tensile testing to failure) of samples along the direction parallel to the tensile axis. The specimens were mechanically polished from both sides to a final thickness of about 60 μm, and polished with diamond paste. Finally, the foils were thinned using a double-jet electrolytic polisher at a voltage of 32 V and a temperature between -10 and -5°C. Analysis of the strained samples was performed using a Tecnai G2 20 microscope, operating at an accelerated voltage of 200 kV.

2.3. Mechanical properties tests

Dog-bone shaped specimens were cut from the middle of the steels along the rolling direction (RD) using electron discharge machining and mechanically polished using the silica paper to the sample dimensions of 15 × 3 × 1.5 mm^3. Conventional tensile tests were conducted using a CMT 5105 pc-controlled mechanical testing system (MTS Co. Ltd, USA) at a constant crosshead speed of 5 × 10^{-3} mm·s^{-1} at room

temperature. During loading, an extensometer was used to measure the sample strain.

2.4. In situ neutron diffraction testing

Neutron diffraction measurements were performed during tensile deformation to study the evolutions of peak intensities and lattice parameters in the steels using a residual stress neutron diffractometer (RSND) at the China Mianyang Research Reactor (CMRR). The diffractometer operates in a time-of-fly (TOF) diffraction mode using neutron pulses with a range of wavelengths, ~0.5–8.0 Å, that travel a distance of 10 m toward the sample before being elastically scattered. The dimensions of the dog-bone specimen for the in situ test was 60 mm long by 15 mm wide by 1.5 mm thick. The specimen was cut from the middle of the as-annealed steel sheet along the RD using electric discharge machining and was chemically cleaned using a mixture of 70 volume percent (vol. %) HCl and 30 vol. % HNO_3. Figure 1a shows the sample position for measurements of lattice strain distributions during in situ tensile loading. The sample was strained in a testing frame with a load capacity of ±100 kN at room temperature. As shown schematically in Fig. 1b, the loading axis was oriented horizontally at 45° to the incident beam. The two detector banks (i.e., $Q_{//}$ – axial; $Q_{\perp}$ – radial) allowed simultaneous collection of the time-resolved diffraction patterns at fixed horizontal scattering angles of ± 90°. The neutron gauge volume was 4 mm in the scattering plane and 2 mm out of the scattering plane and was centered at the specimen axis. Two powder diffraction patterns were recorded by respective detector banks at temporary hold points during the tensile test. Subsequently, the patterns were analyzed for the position and the integral intensity of individual diffraction peaks, from which

the response of lattice strains to the applied stress could be determined. The intergranular strain of the *hkl* grain family can be evaluated from the shift in the diffraction profile.

A wavelength of 1.587 Å was used for the diffraction experiment. Four crystallographic planes for the Fe grains were scanned, namely, (011), (002), (112), and (022) planes. For each scan, the incident and diffracted slits were set with the opening of the same size (approximate $8 \times 8 \times 2$ mm^3), ensuring the same volume of samples was covered by the neutron beam. During each scan, the scattering vector ($\boldsymbol{q}$) was always parallel to the RD (also the length direction) of the sample through the rotation of sample table. With this measurement layout, the crystallographic plane perpendicular to the loading axis was measured at a series of load (or stress) increments, as shown in Fig. 1b.

During the neutron diffraction measurement intervals, the macroscopic strains monitored by an extensometer were held constant. The extensometer has a gauge length of 12.5 mm, and it was centered at the gauge center in the diffractometer plane. The experiment was carried out in load control mode in the elastic region and switched to displacement control shortly before reaching the yield point. The relative lattice strains along the normal direction of individual *hkl* planes were determined with respect to the initial interplanar spacing by

$$\varepsilon_{hkl} = \frac{d_{hkl} - d^0_{hkl}}{d^0_{hkl}}, \tag{2}$$

where d_{hkl} and d_0 are the interplanar spacings of the specified *hkl* planes with and without an external load, respectively. The interplanar spacing was derived from the

diffraction peak position via Bragg's law, which was obtained from peak fitting using a Gaussian function convolved with a sharp-edged exponential. As shown in Figure 1, the indices of LD and TD denote the loading (note that LD is parallel to RD) and transverse directions (LD and TD) of the sample, respectively.

3. Results and discussion

3.1 Microstructural characterization of the as-prepared steels

Microstructural characterization shows that the CG steel has a grain size of ~50 μm, with a ferritic matrix (in grey), and pearlite phase (in black) (Fig. 2a). The pearlite reveals a stratified complex with alternating overlying ferrite and cementite lamellae. Using equation (1), the volume fraction (f_v) of cementite was estimated as ~15%. Conversely, the M steel mainly consists of blocks and laths, which are typical martensitic features (Fig. 2b). EBSD orientation maps reveal the average grain size for the UFG steel is ~ 430 nm (Fig. 2c). One can clearly see that the grains in the UFG steel exhibit a partially recrystallized structure, characterized by some elongated grains. The volume fractions of the high-angle-grain-boundary (HAGB) and low-angle-grain-boundary (LAGB) of the UFG steel are quantified as 40% and 60%, respectively. Here, the misorientation angle above 15° is identified as the HAGB, and those above 2° and below 15° as the LAGB. The ultrafine grains were predominately separated by the HAGB, as illustrated by the black lines in the EBSD maps (Fig. 2c).

The relatively low volume fraction of HAGB in the UFG steel should be associated with its processing history, which includes warm rolling plus low-

temperature annealing at 550°C. Further SEM analysis reveals that numerous light nanoparticles coexist with ultrafine ferritic grains in the UFG steel (Fig. 2d). TEM morphology of UFG steel indicates that numerous nanosized precipitates embed in the ferritic matrix. Statistical analyses revealed that the average size of the nanoparticles is ~ 70 nm (Fig. 2e), with a corresponding f_v of 10.5%. They were mainly identified as cementite (Fe_3C) in a previous study [22].

Neutron diffraction was carried out on the M steel and UFG steel to explore their microstructural features in detail. Four peaks for each steel are shown in Fig. 3, along with the fitted curves using a Gaussian function. Compared to M steel, the intensities of the (011) and (022) peaks for the UFG sample are significantly enhanced, as shown in Fig. 3a and 3d, suggesting that the (011)//RD texture can be attributed to warm rolling. The texture components along the α and γ orientation distribution lines, such as {112}<110> and {001}<110>, are dominant, which should be associated with the formation of cubic texture in the UFG sample as a result of the partial recrystallization during annealing after severe plastic deformation during warm rolling.

Next, each peak for the two steels in Fig. 3 was fitted with a Gaussian function to obtain the peak position. The lattice parameter (a) was then calculated using Bragg's law, $\lambda = 2d\sin\theta$, where d is the interplanar distance of the lattice planes (hkl), with λ and θ representing the wavelength and scattering angle, respectively, and the diffraction angle θ obtained through peak fitting. The planar spacing d for each reflection (hkl) was then calculated using the Bragg equation. The lattice parameter (a) was finally calculated by the following equation for the cubic structure: $d = a/(h^2 + k^2$

$+ l^2)^{1/2}$. Therefore, in calculating the lattice parameter, the error is mainly attributed to θ, which depends on the accuracy of the neutron diffraction measurement. For some peaks of relatively low intensity (e.g., (002) and (022) for the M steel), the error of the peak position is relatively large, which consequently results in a relatively large error in lattice parameter. The calculated lattice parameters for each reflection (*hkl*) and full widths at half maximum (FWHM) of diffraction profiles are shown in Fig. 4 and listed in Table 1.

Compared with other peaks, the calculated lattice parameter error for the (002) peak fitting is slightly larger due to the relatively low intensity and statistics. The averaged lattice parameters for the M steel and UFG steel are estimated to be 2.868 ± 0.001 Å and 2.864 ± 0.001 Å, respectively. One can clearly see that the lattice parameters of the UFG steel are smaller than those of the M steel. The decreasing lattice parameter could result from the decreased amount of interstitial carbon atoms in the Fe lattice after the UFG treatment, including the warm rolling and annealing processes. As demonstrated by the previous study, numerous Fe_3C particles formed in the UFG steel due to the precipitation of carbon in the matrix [22].

The dislocation density in the M steel and UFG steel can be estimated based on the modified Williamson–Hall plot [28]. According to the theory, dislocation can cause line broadening, and the degree of broadening is a function of the contrast factor *C,* which depends on the relative positions of the diffraction vector, Burgers vector, and line vectors of the dislocations, as well as the elastic constants of the crystal [28]. Therefore, the dislocation density can be obtained by relating the broadening-related

term to the contrast factor C, as follows:

$$\cos\theta \bullet \Delta\theta = 0.89\lambda / 2D + (\pi b^2 / 2A)^{1/2} \rho^{1/2} (\sin\theta \bullet C^{1/2}) \ , \qquad (3)$$

where θ is diffraction angle, 0.89 is the FWHM of diffraction profiles, λ is the wavelength of X-rays, D is grain size, b is Burgers vector, A is a function related to circumscribed radius of dislocation, ρ is dislocation density, and C is a contrast factor. Figure 5 shows the relationship of $\cos\theta \cdot \Delta\theta$ and $\sin\theta \cdot C^{1/2}$ for the two steels, the results of which are shown in Figs. 3 and 4 and Table 1. The slopes (K) for the two steels in Figure 5 can be obtained by fitting through the data points, and they can then be used to calculate the dislocation density using the following equation:

$$\rho = 2AK^2 / \pi b^2 . \qquad (4)$$

The thus-estimated dislocation densities for M steel and UFG steel are 2.59×10^{14} cm^{-2} and 1.76×10^{12} cm^{-2}, respectively. These results are well supported by metallurgical principles, and the low dislocation density in UFG steel should be associated with the annealing process after each warm rolling pass.

To further explore the microstructural details, small-angle neutron scattering was performed on the M steel and UFG steel. Because of the strong magnetic propeties of the steels, small-angle neutron scattering was conducted by applying an external magnetic field (1.7 Tesla) along the RD of the specimens to distinguish the neutron scattering signal from that of magnetism. The relationship between intensity and scattering vector (q) is shown in Fig. 6. Before applying the magnetic field, no obvious difference can be seen between M steel (Fig. 6a) and UFG steel (Fig. 6b), and the two steels exhibited isotropy. However, the microstructural features of two steels are

significantly different after applying the magnetic field. The M steel showed weak anisotropy, illustrated by an almost flat ellipse (in blue) with a relatively uniform shell (in yellow) (Fig. 6c), while the UFG steel revealed strong anisotropy exhibited by a significantly flat ellipse (in blue) with an asymmetrical shell (in yellow) (Fig. 6d). The deduced relationship between scattering intensity and q for the two steels is shown in Figs. 6e and 6f, respectively. Along the vertical direction, no obvious difference is observed due to the disturbance of magnetic scattering. Nevertheless, a small deviation can be noted at $q = 0.1$ nm^{-1} for the UFG steel, indicated by an arrow (Fig. 6f) for the horizontal direction. This feature should be the result of the numerous nanosized carbide precipitates in the UFG steel, which is in good agreement with the results of the SEM and TEM analyses (Fig. 2). Wang et al. recently reported similar results using small-angle neutron scattering to study nano-precipitation in a V-containing HSLA steel [29]. They also proved that the deviation at $q = 0.1$ nm^{-1} arises from the formation of nanoscale ($d \leq 50$ nm) vanadium carbide (VC) precipitates during the isothermal hold.

3.3 Comparison of tensile properties

Figure 7 shows typical true tensile stress–strain curves for the UFG steel and M steel, compared with that for the annealed CG steel (grain size 50 μm). Obviously, the UFG steel and the M steel exhibit significantly higher strength than their CG counterpart. For the UFG steel, the tensile yield strength σ_y (at 0.2% offset) reaches as high as 1250 MPa, and the ultimate tensile strength (σ_{UTS}) is 1400 MPa, both of which are remarkably higher than those of the CG steel (σ_y is 380 MPa and σ_{UTS} is 880 MPa).

The M steel reveals the highest strength values (σ_y is 1290 MPa and σ_{UTS} is 1660 MPa) of all three samples. However, its elongation-to-failure (ε_f) is as low as 7%. In contrast, the UFG steel exhibits an ε_f as high as 15%. It has been well established that a product of high strength and ductility is attractive for structural applications in high impact energy absorption. The product of σ_{UTS} and ε_f for the UFG steel is as high as 21 GPa%, which is nearly double the value for M steel (11.6 GPa%) and considerably higher than that for CG steel (17.6 GPa%) with the same chemical compositions.

3.4 In situ neutron diffraction during uniaxial tension

Neutron diffraction patterns of (110), (002), and (112) planes in the M steel and UFG steel during tensile tests are shown in Fig. 8(a–a2) and Fig. 8(b–b2), respectively. As the load levels increased (indicated by arrows), the intensities of the peaks slightly decreased and the peak position shifted to the left for both steels.

Figure 9 shows the evolution of lattice strain as measured by in situ neutron diffraction for the M steel (a–a1) and the UFG steel (b–b1) during tensile loading. For the M steel, lattice strain of the (110), (002), and (112) planes increases linearly with stress from null to 1500 MPa. However, a strong dependence on orientation was observed in the different planes' elastic microstrains, and obvious anisotropy can be observed from the elastic strains of different lattice planes. The modulus for the (002) grains is the lowest, and the modulus for the (112) grains is the highest, suggesting that the former is soft and the latter is hard (Figs. 9a). This trend might be associated with the blocky microstructure of martensite in the M steel. Interestingly, UFG steel shows a significantly different response, which is nearly isotropic under initial tensile loading (Fig. 9b). One can clearly see that the strains of the (110), (002), and (112) planes are

nearly identical with increasing stress from 0 to 450 MPa. Above 450 MPa, however, the increase in lattice strain of the (110) plane becomes smaller than that of the (002) and (112) planes, suggesting that the nanosized carbide selectively increases the elastic modulus of the (110) lattice at this stage compared to the other two planes. As mentioned above, the UFG steel has a partially recrystallized microstructure, meaning that a certain number of (mobile) dislocations in the microstructure existed prior to the mechanical testing. The preexisting dislocations can be expected to significantly affect the yield behavior. However, the results shown in Fig. 6b suggest that the nanosized carbides contributes to the hardening ability even within the elastic region. One possible explanation would be the high degree of elastic anisotropy of cementite, which has been demonstrated by both experimental observations [30] and first principles calculations [31]. We postulate that local rotation of the nanosized carbide could occur at this elastic deformation stage such that the elastic anisotropy of the cementite contributes to the increased elastic modulus of the (110) lattice. During plastic deformation, the nanosized carbides in the spheroidized microstructure could further increase the work hardening rate by promoting the accumulation of geometrically necessary dislocations around the particles [21], and this is the direction of our future studies on this material.

Generally speaking, the diffraction measurement provides a diffraction-averaged lattice strain value for all the grains that contribute to the diffraction peak. The local stress state in a particular grain depends on both its orientation (related to the influence of elastic and plastic anisotropy) and the surrounding grains to ensure the

continuity of the deformation field. This may lead to stress inhomogeneities within the grain and also cause a deviation from the collective behavior of the same *hkl* family. However, such a stress variation for grains within the same family is expected to be local and much smaller than that caused by the anisotropic properties.

Figure 9b1 shows the in situ neutron diffraction measurement of the lattice strain evolution with respect to macroscopic strain during tensile deformation of the UFG steel. Similar to the results shown in Fig. 9b, nearly isotropic behaviors are measured for all the three planes for the initial loading stage. Above macrostrain levels of 0.3% (corresponding to the stress level of 450 MPa), the increase in lattice strain for the (110) plane starts to slow down compared to the (112) and (002) planes. Interestingly, when the macroscopic strain goes beyond 0.5% (i.e., stress above 1200 MPa), lattice strains for the {112} reflection decrease remarkably along LD, while those for the {110} and {002} planes remain unchanged. This decrease in the lattice strains for the {112} reflection corresponds to a global stress drop (Fig. 9b), which is typically referred to as the yield-point-elongation (YPE), and is also shown in the tensile stress–strain curve in Fig. 7. In terms of deformation mode, YPE typically involves a propagative localized plastic band traveling along the specimen length. The results in Fig. 9b1 indicate that the "softening" of the UFG steel occurs preferentially on the (112) plane, while the lattice strains of the (110) and (002) planes remain unchanged between the last two recorded measurement steps. Hence the plastic instability associated with the YPE in the UFG steel is the result of the competition and compatibility between the load shedding of the (112) planes and the continued load

bearing of the (110) and (002) planes. In contrast, no YPE is shown in Fig. 7 for the M steel and no reverse of lattice strain was observed for the M steel counterpart (Fig. 9a1).

Moreover, the load transfers from the "softer", plastically deformed grains, such as the {220} and {111}, to the {i002} grains with the increase in plastic strain (Figs. 9a1, b1). Theoretically, the normal to {002} planes are the most compliant crystallographic direction. Consequently, the strains measured for the {200} reflection are the highest. Hence, the {002} grain is much easier to deform.

Figure 10 shows the TEM micrographs of the UFG steel before (a) and after deformation (b, c). Postmortem TEM observations showed that the dispersive nanoparticles should be effective obstacles to the movements of dislocations during deformation (Fig. 10). Before deformation, Fig. 10a reveals that numerous very fine precipitates (with several nanometers in diameter) coexist with several large particles (indicated by arrows), which were proved to be cementite (Fe_3C) particles with an average diameter of 70 nm [23]. It has been reported that vanadium carbide is often selected as an interphase precipitate, and a relatively large amount of VC precipitation occurs in ferrite during cooling [29]. The planar rows of particles (indicated by broken lines) should be the VC precipitates, which are typically small in size (< 20 nm), possibly being formed by interphase precipitation [29]. In Fig. 10b and c, the edges of the Fe_3C particles are very blurred because of the significant pile-up of dislocations, as indicated by arrows and a triangle. Here, hard cementite particles act as obstacles to dislocation slip in ferrite, leading to dislocation pile-up at the cementite/ferrite interface. For a finer particle, significantly higher stress is required to make

dislocations pass through the particle boundary via cross-slip compared with a larger particle deformed at the same temperature. Hence, the strength of steel typically decreases with increasing particle size [32, 33]. Furthermore, the present study suggests that the nanosized particles promote plastic deformation of UFG steels by enabling dislocation slip near the particles. We hypothesize that there exists an optimum combination of the ferrite grain size and cementite particle size and volume fraction for the desired strength and ductility of the steel. Atomistic-scale simulations have suggested that the hetero-interface within duplex structures provides a strong interatomic bonding strength [34, 35]. Accordingly, numerous dislocations can cut into the brittle phase. In this work, TEM observations clearly indicated that the incoherent interface between nanosized Fe_3C particles and ferritic matrix acted as a strong barrier to dislocation motion, which led to stress concentration at the edges of the particles.

The classic H-P relation can describe the strengthening effect of various factors in metallic materials [36]. Because stress can be divided into several terms, including grain size hardening (σ_{gs}), solid-solution hardening (σ_{sh}), precipitation hardening (σ_{ph}), and dislocation hardening (σ_{dh}), the H-P relation can be rewritten as

$$\sigma_y = \sigma_0 + \sigma_{gs} + \sigma_{sh} + \sigma_{ph} + \sigma_{dh} \ , \quad (5)$$

where σ_y represents yield stress, and σ_0 is the Peierls-Nabarro stress. In this study, the terms of σ_{gs}, σ_{ph} and σ_{dh} are of interest.

For the UFG steel, work hardening is mainly derived from the nanosized precipitates in addition to grain refinement. As nanosized precipitates block the dislocation motion inside the crystallites, their strengthening effect, σ_{ph}, can be used

to estimate the yield-strength contribution due to the precipitation alone, based on the well-known Ashby-Orawan model [29, 37]:

$$\sigma_{ph} = \frac{0.538Gbf_v^{0.5}}{2R} ln(R/b) \ , \quad (6)$$

where G is the shear modulus (~76 GPa), b is Burgers vector (2.85 $\times 10^{-10}$ m), f_v is the carbide volume fraction, and R is the mean precipitate radius. Obviously, a decrease in the precipitate size and an increase in the precipitate volume fraction lead to the increase in the strength of the studied alloys. Previous TEM observations showed that average size of the spherical particles was 70 nm, and high-resolution TEM proved that the particles were cementite and incoherent with the ferrite matrix in UFG steel [22]. Using equation (1), the volume fraction of the carbide phase has been estimated as $f_v \approx$ 10.5% (Figs. 2d and e). Because the precipitates preserve a phase totally different from that of the matrix, the increase in yield strength from the precipitates is determined using Eq. (4) to be as high as 270 MPa. Therefore, the high strength in the UFG steel originates significantly from the strengthening effect of the high density of the nanosized carbides.

Neutron diffraction results also indicate different dislocation densities in the UFG ferritic steel (1.76×10^{12} cm^{-2}) and the fully martensitic steel (2.59×10^{14} cm^{-2}). The yielding behavior should be closely related to the behavior of mobile dislocations which could already exist in either UFG ferritic or M steels. The strengthening effect from the preexisting dislocations, σ_{dh}, can be estimated by

$$\sigma_{dh} = \alpha Gb\sqrt{\rho} \ , \quad (7)$$

where α is a parameter with value of 0.5 for edge dislocations and 1.5 is the value of

screw dislocations. The deduced values are 3.49 × 10^6 Pa and 2.87× 10^5 Pa, respectively, for M steel and UFG steel because of the large preexisting dislocation density.

Finally, one should note that the intensities of the (011) and (022) peaks for the UFG sample are significantly enhanced compared with the M steel. The components along the α and γ orientation distribution lines, such as {112}<110> and {001}<110>, are dominant and associated with the formation of cubic texture in the UFG sample resulting from partial recrystallization. This kind of orientation is prominent in bcc rolling textures and is responsible for the good ductility. The increasing deformation levels shift the peak intensity in a fiber from {001}<110> towards {112}<110> [38]. For example, a well-developed {112}<110> recrystallization texture is formed by cold rolling for a Ti-base shape memory alloy, and it has been attributed to the enhanced superelasticity along the RD [39]. This study has provided quantitative insights into the strengthening mechanisms by the nanoscale precipitates in the UFG steels, and the results here may shed lights on the design of new steels as well as the development of innovative processing parameters.

4. Concluding remarks

The microstructures and mechanical properties of low-alloy medium-carbon steel with a duplex microstructure composed of nanoscale spheroidized Fe_3C in ultrafine-grained (UFG) ferritic steel were characterized using in situ neutron diffraction during uniaxial tension. Postmortem EBSD analyses and TEM observations were also used to elucidate the relationship between the mechanical properties and

microstructures of the steel. The major results are summarized as follows:

(1) Compared to the as-prepared martensitic (M) steel, the intensities of the (011) and (022) peaks for the UFG sample are significantly enhanced, suggesting that the (011)//RD texture is the result of the warm rolling process. The components along the α and γ orientation distribution lines, such as {112}<110> and {001}<110>, are dominant and associated with the formation of cubic texture in the UFG sample, resulting from partial recrystallization during annealing after severe deformation during warm rolling.

(2) The UFG steel reveals significantly different lattice strain responses and is nearly isotropic under initial tension. The lattice strains of (110), (002), and (112) planes are identical for stresses from 0 to 450 MPa. The increase of lattice strain of the (110) plane becomes smaller than that of the (002) and (112) planes as the stress increases beyond 450 MPa, suggesting that the nanosized carbides (which include cementite and microalloy precipitate, i.e. vanadium carbide) contribute to the increase of elastic modulus of the (110) lattice more than to the other two planes. We postulate that this is due to the elastic anisotropy of the nanosized carbides and the grain rotation of the nanosized precipitates. For the M steel, on the other hand, the modulus of the (002) grain is lower than that of the (112) and (110) grains, verifying the crystallographic theory that the {002} planes are the most compliant direction.

(3) There are different dislocation densities in the UFG ferritic steel (1.76×10^{12} cm^{-2}) and the fully M steel (2.59×10^{14} cm^{-2}). The strengthening effects of the UFG steel are mainly attributed to the nanosized precipitates and grain refinement,

whereas that of the martensitic steel is dominated by the preexisting dislocations. The nanosized carbides could increase work hardening rate by promoting the accumulation of geometrically necessary dislocations around the particles which act as barriers to dislocations.

Acknowledgments

This project is supported by NSAF (Grant No. U1430132), the Natural Science Foundation of China (NSFC) (Grant No. 51574079), and the Science and Technology Research Project of Education Department of Liaoning Province (L20150177). Oak Ridge National Laboratory is operated by UT-Battelle, LLC, for the U.S. DOE under contract DE-AC05-00OR22725. The US government retains and the publisher, by accepting the article for publication, acknowledges that the US government retains a nonexclusive, paid-up, irrevocable, worldwide license to publish or reproduce the published form of this manuscript, or allow others to do so, for US government purposes.

References

[1] L. Lu, Y. F. Shen, X.H. Chen, L.H. Qian, K. Lu, Ultrahigh strength and high electrical conductivity in copper, Science, 304 (2004) 422–426.

[2] Y. Kimura, T. Inoue, F. Yin, K. Tsuzaki, Inverse temperature dependence of toughness in an ultrafine grain-structure steel, Science 320 (2008) 1057.

[3] S. Maropoulos, N. Ridley, S. Karagiannis, Structural variations in heat treated low alloy steel forgings, Mater. Sci. Eng. A380 (2004) 79–92.

[4] A.R. Mirak, M. Nili-Ahmadabadi, Effect of modified heat treatments on the microstructure and mechanical properties of a low alloy high strength steel, Mater.

Sci. Technol. 20 (2004) 897–902.
[5] R. Song, D. Ponge, D. Raabe, Mechanical properties of an ultrafine grained C–Mn steel processed by warm deformation and annealing, Acta Mater., 53 (2005) 4881–4892.
[6] Y.W. Lee, Y.I. Son, S. J. Lee, Microstructure and mechanical properties of spheroidized D6AC steel, Mater. Sci. Eng. A 585 (2013) 94–99.
[7] A. Salemi, A. Abdollah-zadeh, M. Mirzaei, H. As-sadi, A study on fracture properties of multiphase microstructures of a Cr-Mo steel, Mater. Sci. Eng. A 492 (2008) 45–48.
[8] A. Abdollah-zadeh, A. Salemi, H. Assadi, Mechanical behavior of Cr–Mo steel with tempered martensite and ferrite–bainite–martensite microstructure, Mater. Sci. Eng. A, 483–484 (2008) 325–328.
[9] G. Krauss, Steels-Processing, Structure, and Performance, ASM International, Materials Park, OH, 2005, pp.251–262.
[10] H.K.D.H. Bhadeshia, Steels for bearings, Prog. Mater. Sci. 57 (2012) 268–435.
[11] M. Song, K. Guan, Failure analysis of a weld-decayed austenitic stainless steel, Eng. Fail. Anal. 18 (2011) 1613–1618.
[12] L. Ratke, P.W. Voorhees, Growth and coarsening–Ostwald ripening, Material Processing, Springer, New York, NY, 2002, pp.117–166.
[13] D. Lian, Microstructure properties of tempered D6ac steel, Appl. Surf. Sci. 264 (2013) 100–104.
[14] P.K. Liaw, M.G.Peck, G.E. Rudd, T.K. Lai, Fatigue crack growth behavior of D6AC space shuttle steel, Eng. Fract. Mech. 43 (1992) 379–400.
[15] S.C. Wu, H.C. Wen, M.J. Wu, C.P. Chou, Fracture responses of microstructures of electron beam-welded D6AC, Vacuum 86 (2012)1828–1833.
[16] D.M. Lian, Microstructure properties of tempered D6AC steel, Appl. Surf. Sci. 264 (2013) 100–104
[17] M. Jahazi, G. Ebrahimi, The influence of flow-forming parameters and microstructure on the quality of a D6ac steel, J. Mater. Process. Technol. 103 (2000) 362–366.

[18] T. Suzuki, Y. Ono, G. Miyamoto, T. Furuhara, Effects of Si and Cr on bainite microstructure of medium carbon steels, ISIJ Int. 50 (2010) 1476–1482.

[19] K. Notvest, Effect of thermal cycles in welding D6AC steel, Weld. J. 45 (1966) 173S–177S.

[20] H. Ghaffarian, A.K. Taheri, S. Ryu, K. Kang, Nanoindentation study of cementite size and temperature effects in nanocomposite pearlite: A molecular dynamics simulation, Curr. Appl. Phys. 16 (2016) 1015–1025.

[21] J. Kadkhodapour, S. Schmauder, D. Raabe, S. Ziaei-Rad, M. Calcagnotto, Experimental and numerical study on geometrically necessary dislocations and non-homogeneous mechanical properties of the ferrite phase in dual phase steels, Acta Mater., 59 (2011) 4387–4394.

[22] N. Jia, Y. F. Shen, J. W. Liang, X. W. Feng, H. B. Wang, R. D. K. Misra. Nanoscale spheroidized cementite induced ultrahigh strength-ductility combination in innovatively processed ultrafine-grained low alloy medium-carbon steel. Sci. Rep. 7 (2017) 2079.

[23] Y. Tomota, P. Luk, D. Neov, S. Harjo, Y.R. Abe, In situ neutron diffraction during tensile deformation of a ferrite-cementite steel, Acta Mater., 51 (2003) 805–817.

[24] M.A. Weisser, A.D. Evans, S. Van Petegem, S.R. Holdsworth, H. Van Swygenhoven, In situ room temperature tensile deformation of a 1% CrMoV bainitic steel using synchrotron and neutron diffraction, Acta Mater., 59 (2011) 4448–4457.

[25] W. Woo, V.T. Em, E.-Y. Kim, S.H. Han, Y.S. Han, S.-H. Choi, Stress–strain relationship between ferrite and martensite in a dual-phase steel studied by in situ neutron diffraction and crystal plasticity theories, Acta Mater., 60 (2012) 6972–6981.

[26] N. Jia, R. Lin Peng, Y.D. Wang, S. Johansson, P.K. Liaw, Micromechanical behavior and texture evolution of duplex stainless steel studied by neutron diffraction and self-consistent modeling, Acta Mater., 56 (2008) 782–793.

[27] L. Cheng, A. Böttger, T. de Keijser, E.J. Mittemeijer, Lattice parameters of iron-carbon and iron-nitrogen martensites and austenites, Scr. Mater. 24 (1990) 509–

514.

[28] J. Gubicza, G. Ribárik, G.R. Goren-Muginstein, A.R. Rosen, T. Ungár, The density and the character of dislocations in cubic and hexagonal polycrystals determined by X-ray diffraction, Mater. Sci. Eng. A, 309–310 (2001) 60–63.

[29] Y.Q. Wang, S.J. Clark, V. Janik, R.K. Heenan, D. Alba Venero, K. Yan, D.G. McCartney, S. Sridhar, P.D. Lee, Investigating nano-precipitation in a V-containing HSLA steel using small angle neutron scattering, Acta Mater., 145 (2018) 84–96.

[30] A. Kagawa, T. Okamoto, H. Matsumoto, Young's modulus and thermal expansion of pure iron-cementite alloy castings, Acta Mater. 35 (1987) 797-803.

[31] C. Jiang, S.G. Srinivasan, A. Caro, S.A. Maloy, Structural, elastic, and electronic properties of Fe3C from first principles, J. Appl. Phys., 103, 043502 (2008).

[32] M.-X. Zhang, P.M. Kelly, Accurate orientation relationships between ferrite and cementite in pearlite, Scripta Mater 37 (1997) 2009–2015.

[33] C.S. Zheng, L.F. Li, W.Y. Yang, Z.Q. Sun, Relationship between microstructure and yield strength for plain carbon steel with ultrafine or fine (ferrite & cementite) structure, Mater. Sci. Eng. A, 617 (2014) 31–38.

[34] T. Shimokawa, T. Oguro, M. Tanaka, K. Higashida, T. Ohashi, A multiscale approach for the deformation mechanism in pearlite microstructure: Atomistic study of the role of the heterointerface on ductility, Mater. Sci. Eng. A, 598 (2014) 68–76.

[35] S. Goel, S.S. Joshi, G. Abdelal, A. Agrawal, Molecular dynamics simulation of nanoindentation of Fe_3C and Fe_4C, Mater. Sci. Eng. A, 597 (2014) 331–341.

[36] M.A. Mayers, K.K. Chawla, Mechanical behavior of materials. Prentice Hall, Inc. Upper Saddle River, New Jersey 07458. (1999).

[37] R.G. Guan, Y.F. Shen, Z.Y. Zhao, X. Wang, A high-strength, ductile Al-0.35Sc-0.2Zr alloy with good electrical conductivity strengthened by coherent nanosized-precipitates, J. Mater. Sci. Technol., 33 (2017) 215–223.

[38] U.F. Kocks, C.N. Tom, H.-R. Wenk, Texture and anisotropy, Cambridge University Press, UK, 1998.

[39] Y. Fukui, T. Inamura, H. Hosoda, K. Wakashima, S. Miyazaki, Mater. Trans. 45 (2004) 1077–1082.

Tables and Figures

Table 1. The Gauss-fitted peak position and calculated lattice parameter following Bragg's law for the CG and UFG samples.

(*hkl*)		(011)	(002)	(112)	(022)
M-steel	2θ (°)	46.001±0.0028	67.171±0.0103	85.426±0.0061	103.027±0.0173
	a (Å)	2.872±0.001	2.869±0.001	2.865±0.001	2.867±0.001
UFG	2θ (°)	46.049±0.0012	67.256±0.0061	85.554±0.0032	103.399±0.0028
	a (Å)	2.868±0.001	2.866±0.001	2.862±0.001	2.860±0.001

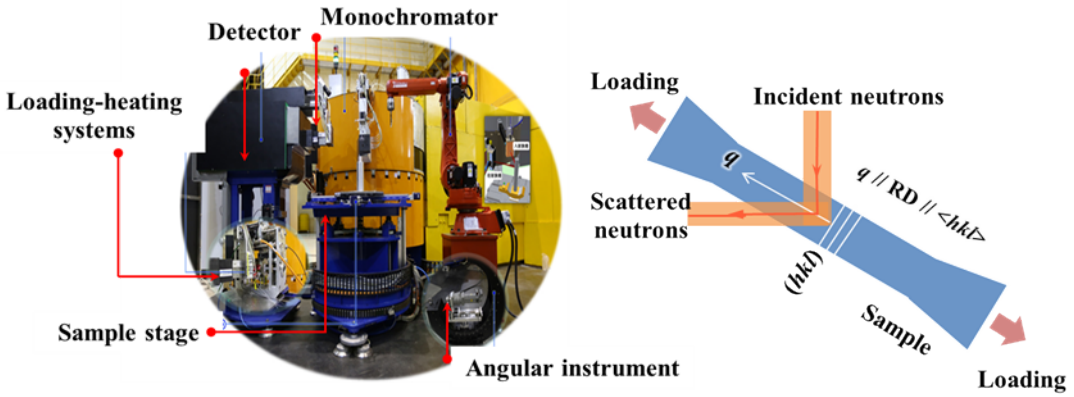

Fig. 1 Schematic illustration of in situ neutron diffraction during the loading of tensile stress: (a) sample position for measurements of lattice strain distributions during in situ tensile loading and (b) the relationship between crystallographic plane and the loading axis in the measurements.

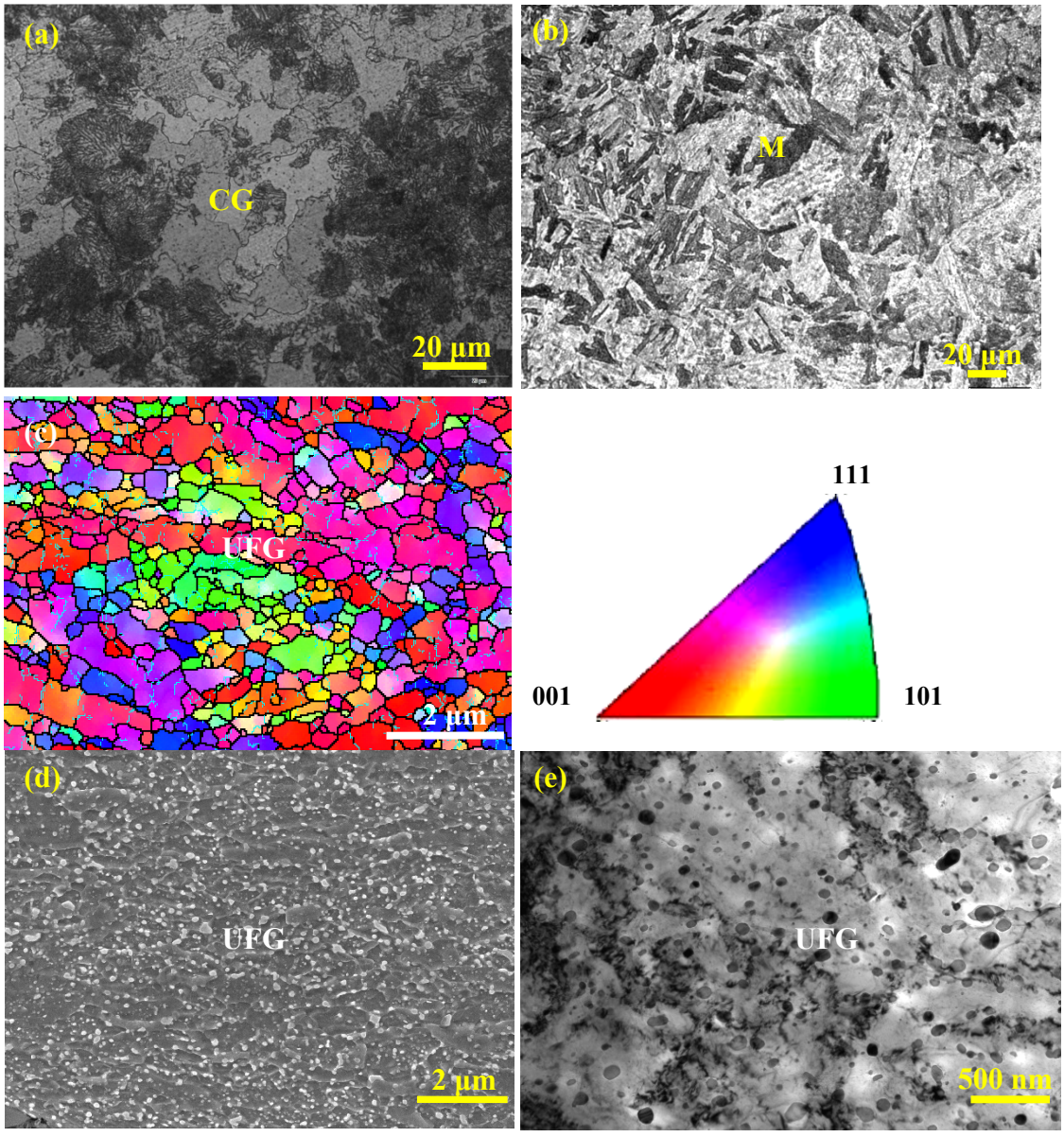

Fig. 2 Metallographical microstructures of coarse-grained (CG) steel indicate that the average grain size is ~50 μm with ferritic matrix and pearlite phase (a); M steel mainly consists of blocks and laths, which are obvious features of martensite (b); EBSD orientation maps for ultrafine-grained (UFG) steel reveal the average grain size is ~430 nm (c); SEM picture shows numerous nanoparticles coexist with ultrafine grains in the UFG steel (d); and TEM morphology of UFG steel indicates that the nanosized

precipitates embedded in the ferritic matrix (e).

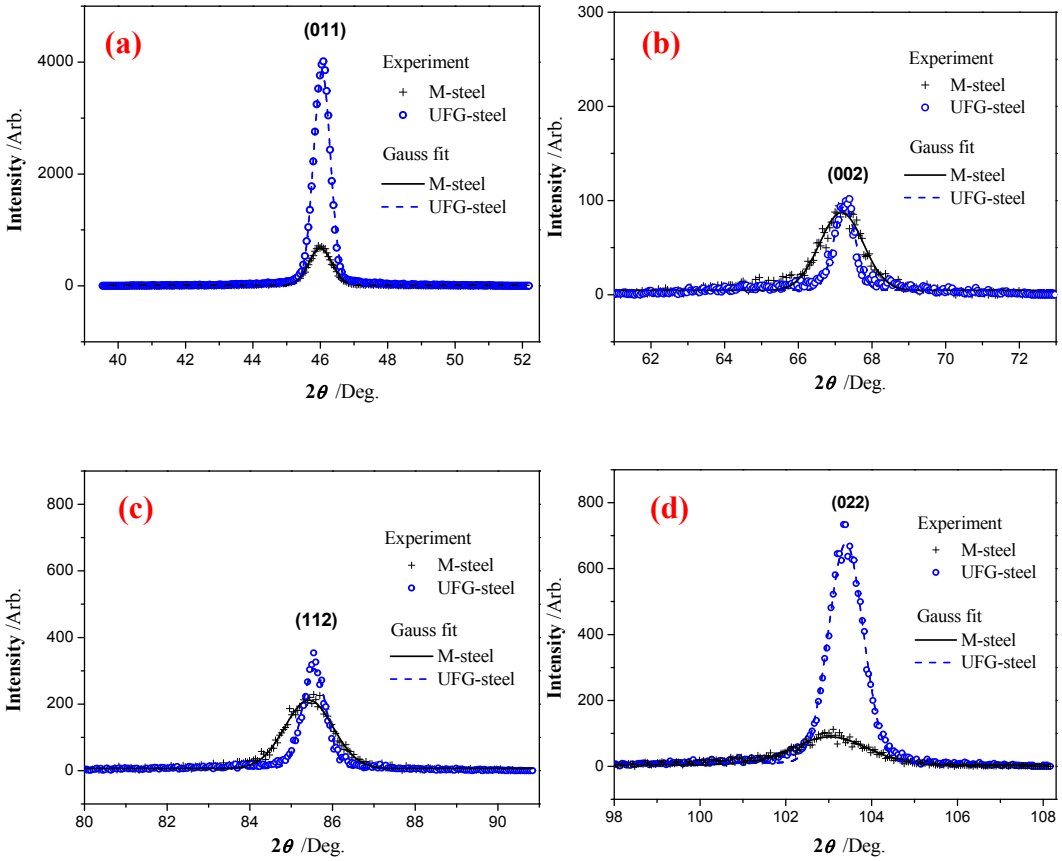

Fig. 3 (a) and (b) show neutron diffraction and Gaussian-fitted patterns of (011), (002), (112), and (022) peaks for the M steel andUFG steel, respectively. The steel has a chemical composition of 1.05Cr-1.01Mo-0.73Mn-0.61Ni-0.17Si-0.09V-0.43C (wt.%).

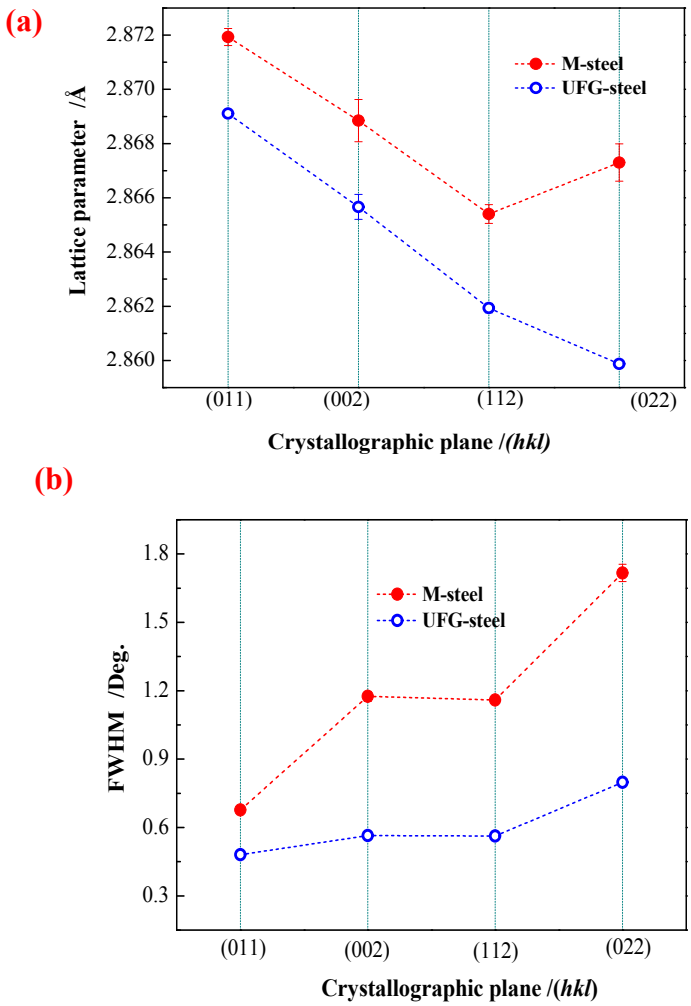

Fig. 4 The calculated lattice parameter (a) and full widths at half maximum (FWHM) of each peak (b) based on Bragg's law for the M steel and UFG steel.

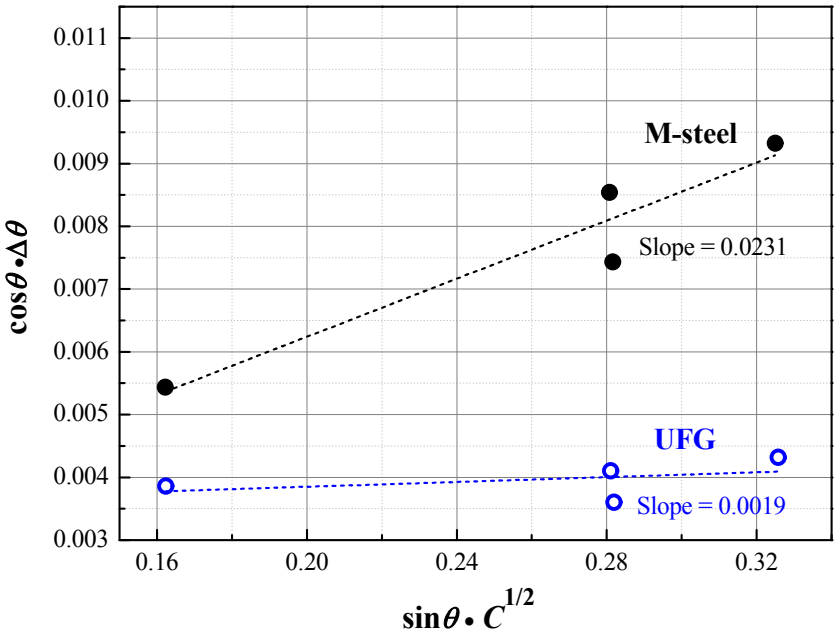

Fig. 5 The estimated dislocation density in the M steel and UFG steel, based on the modified Williamson–Hall plot.

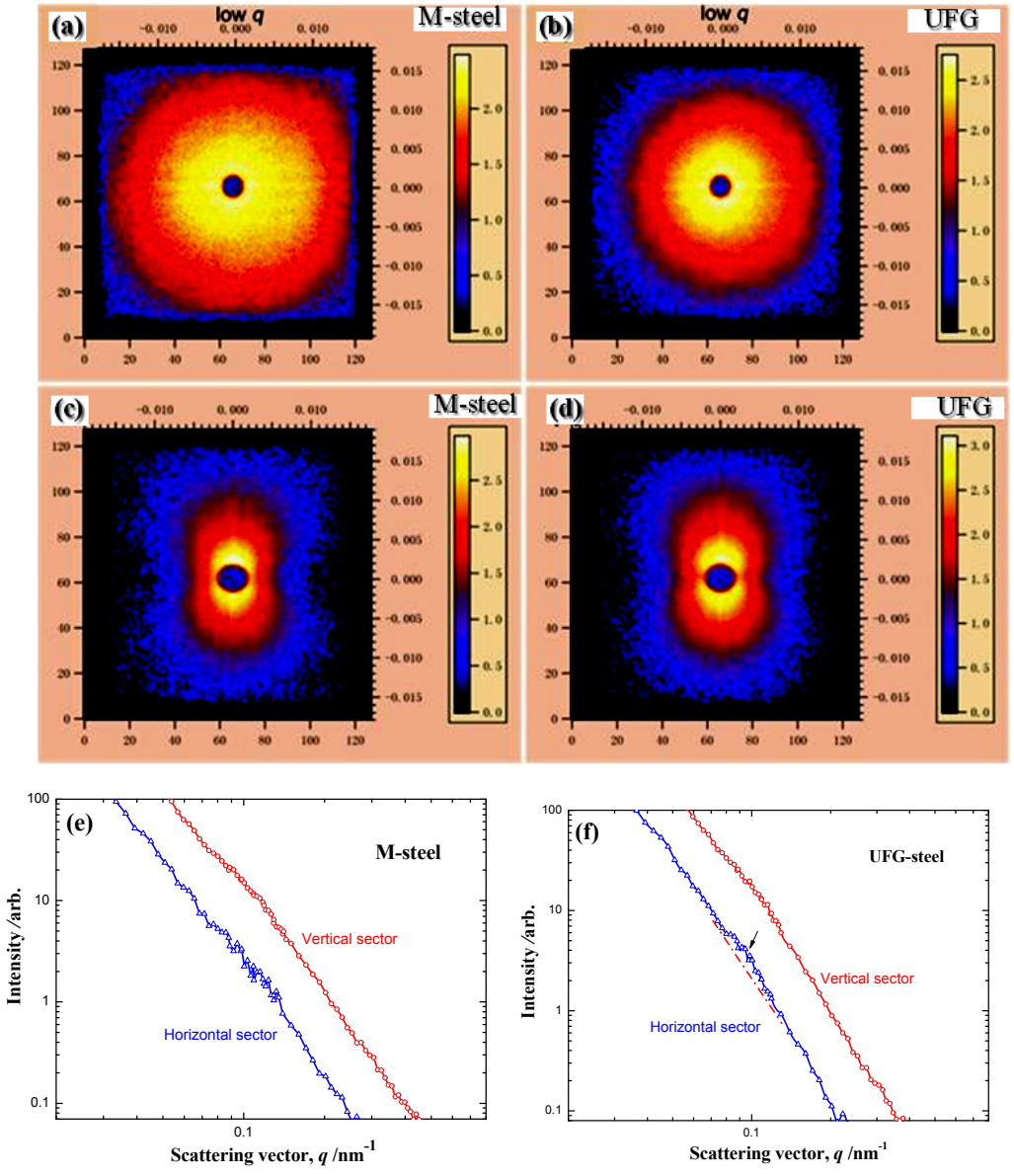

Fig. 6 Two-dimensional maps of small-angle neutron scattering for the M steel (a) and UFG steel (b) and those obtained after applying an external magnetic field (c) and (d), respectively. The corresponding relationships between intensity and scattering vector are deduced along the horizontal and vertical directions for the M steel (e) and the UFG steel (f).

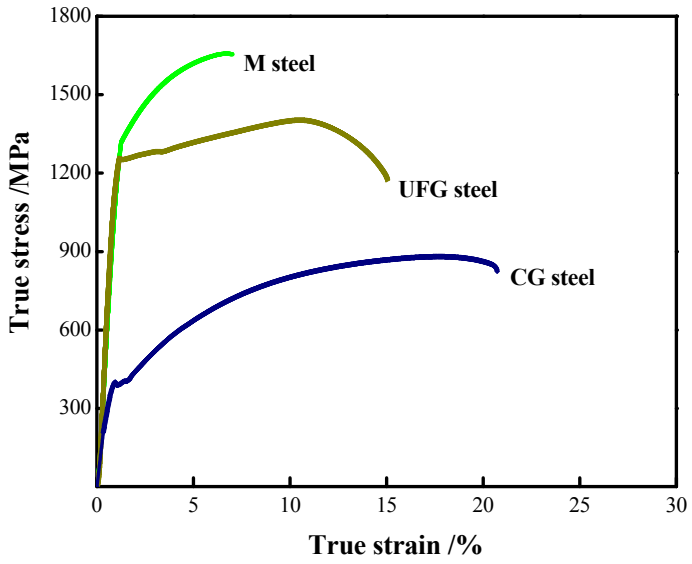

Fig. 7 Tensile true stress–strain curve for the as-prepared UFG steel. For comparison, tensile stress–strain curves for a CG steel and M-steel with identical chemical compositions are also included.

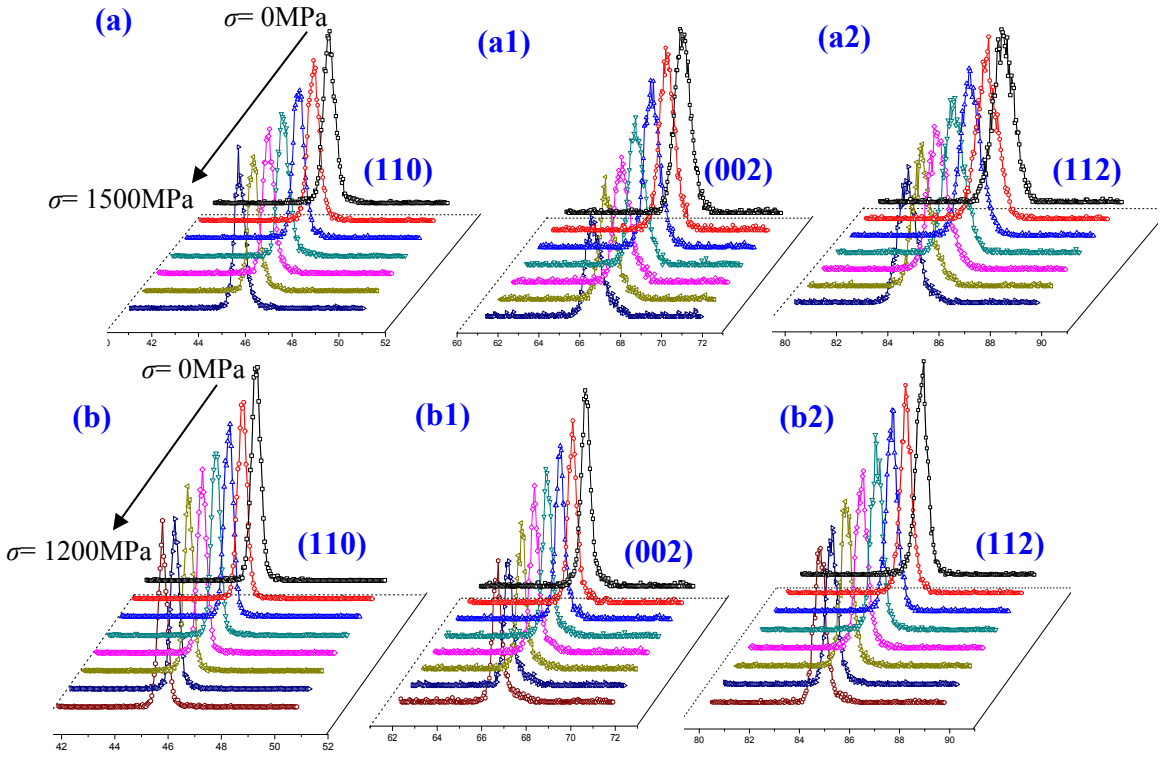

Fig. 8 Variation of peaks intensity during in situ tensile defomration. (a), (a1), and (a2) represent the (110), (002), and (112) planes in M steel, respectively, while (b), (b1), and (b2) represent the corresponding planes in UFG steel, respectively.

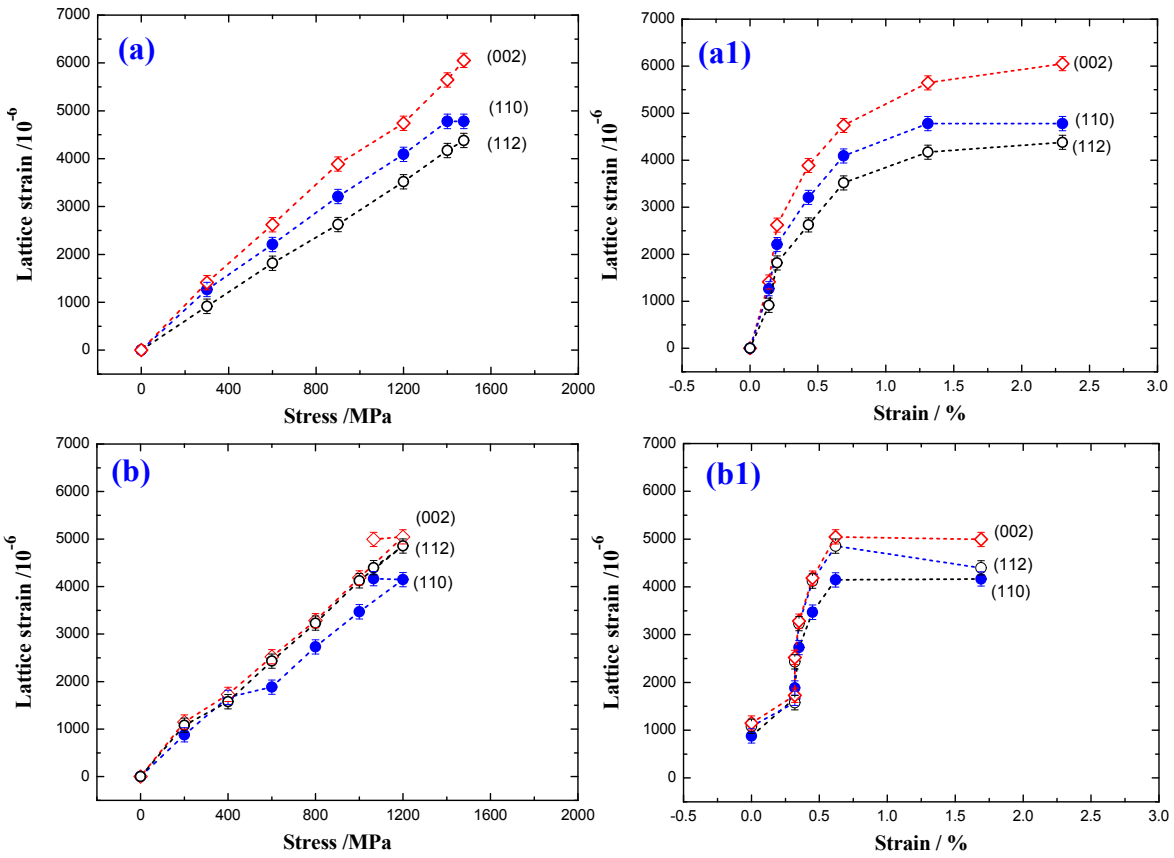

Fig. 9 Neutron diffraction patterns of (011), (002), and (112) planes for M steel (a, a1) and UFG steel (b, b1) during in situ tension along LD.

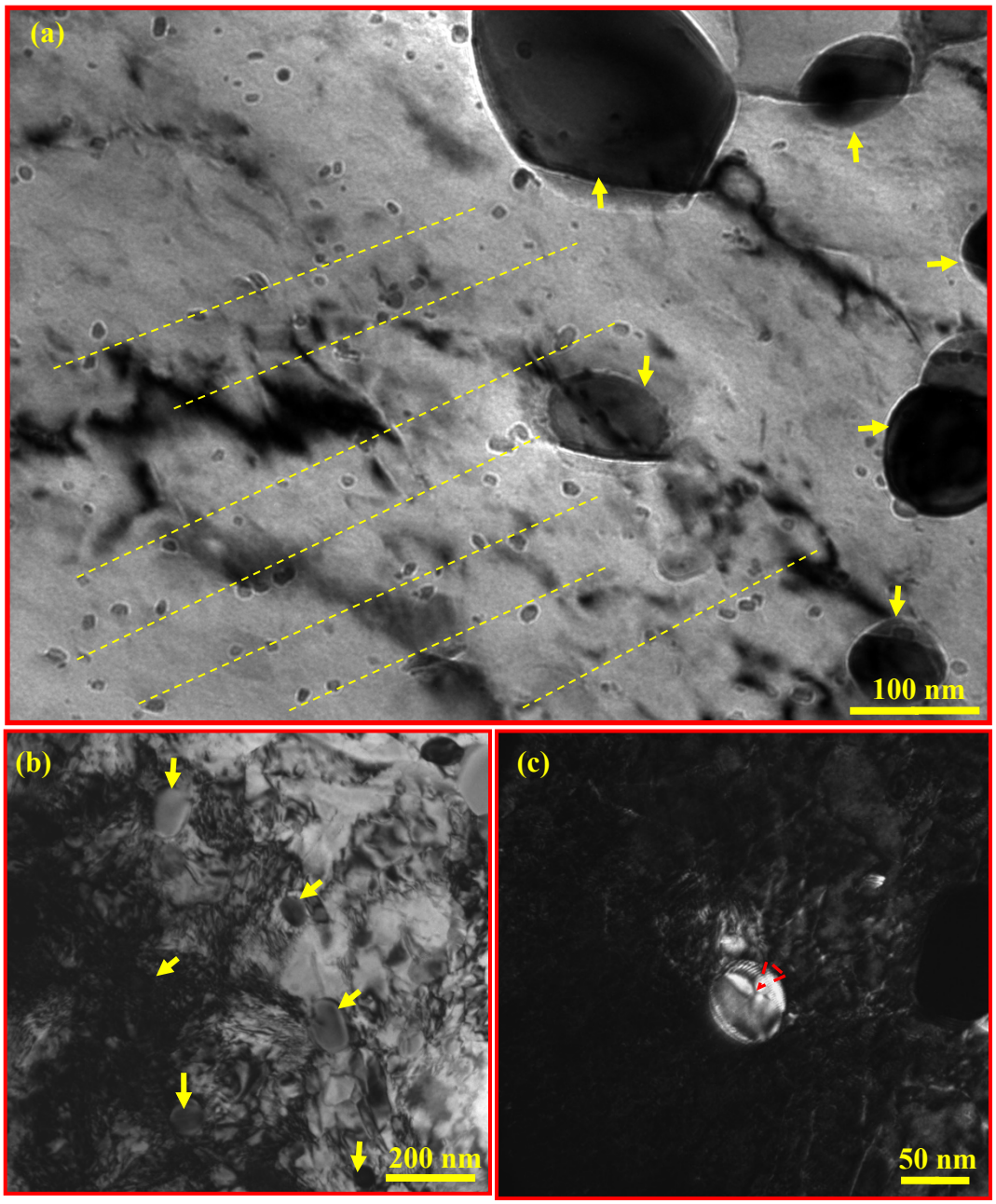

Fig. 10 TEM micrographs showing the morphologies of UFG steels before (a) and after (b, c) tensile deformation. The planar rows of particles indicated by broken lines are the VC precipitates (a), and dense dislocations piled-up around some Fe_3C particles, as indicated by arrows (b). Close observation shows dislocations that accumulated at the edge of nanosized Fe_3C particles. Also shown are some traces of slip in the interior of Fe_3C particle, as indicated by a triangle (c).